Advances in Wind Engineering 3 (2026) 100101

Contents lists available at ScienceDirect

Advances in Wind Engineering

journal homepage: www.keaipublishing.com/en/journals/awe

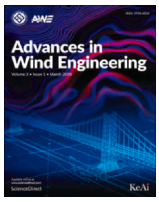

A hybrid physics-informed graph neural network for tornado wind-field modeling

Reda Snaiki*, Seyedeh Fatemeh Mirfakhar

Department of Construction Engineering, École de Technologie Supérieure, Université du Québec, Montréal, Québec, Canada

ARTICLE INFO

Keywords:
Tornado wind field
Graph neural network
Physics-informed machine learning
Large-eddy simulation

ABSTRACT

The accurate prediction of tornado wind fields is paramount for the wind-resistant design of critical infrastructure. Analytical models offer a computationally efficient and physically grounded foundation for representing the primary structure of tornadic vortices. While these models provide valuable approximations, they inherently simplify the highly complex turbulent characteristics observed in tornado phenomena. Conversely, high-fidelity methods like Large-Eddy Simulations (LES) capture these intricate details with high accuracy but are computationally prohibitive for many direct engineering applications. This study introduces a novel hybrid framework that integrates a physics-based analytical model with a physics-informed deep learning model to bridge this gap. The proposed approach incorporates physics in two distinct steps. First, an established analytical model (the Baker model) is utilized to generate a baseline velocity field, providing a robust physical approximation of the vortex. Second, a Graph Neural Network (GNN) is trained to learn the complex, non-linear residuals between this analytical baseline and ground-truth LES data sourced from foundational numerical studies. The GNN architecture is designed to capture spatial interdependencies within the vortex field, with training guided by physics-based penalty functions to ensure physical consistency. The results demonstrate that the hybrid GNN model achieves a global test-set root-mean-square error (RMSE) of 0.0039, a substantial improvement compared to the analytical baseline's test-set RMSE of 0.8384. This framework presents a computationally efficient alternative that preserves the high fidelity of LES mean flow structures, offering a promising tool for advanced engineering analysis and design.

1. Introduction

Tornadoes are among the most violent and destructive weather hazards, causing substantial damage and fatalities each year (Davies-Jones, 2015; Sessa and Trapp, 2020; Hadavi et al., 2022). The extreme wind speeds, coupled with rapid pressure falls, create loading conditions that differ fundamentally from those associated with synoptic-scale winds (Smith et al., 2020; French and Kingfield, 2021; Zhou et al., 2025). Consequently, establishing robust wind-resistant designs for critical infrastructure, such as nuclear power plants and transmission towers, requires accurate, three-dimensional characterization of the internal flow field within these vortices (Zhang et al., 2023c; Zhao et al., 2024; Dong et al., 2025). However, the inherent unpredictability and danger of tornadoes make direct, in-situ measurements of their internal structure exceedingly difficult and limited (Kurdzo et al., 2017; Tochimoto, 2022). This challenge necessitates complementary approaches, such as laboratory simulators and numerical modeling, to represent, reproduce, and study tornadic flows under controlled conditions (Kim and Matsui, 2017; Tang et al., 2018; Wang et al., 2022; Cao and Liu, 2023).

Over the years, various analytical and empirical vortex models have been proposed to provide closed-form or low-parameter descriptions of tornadic winds (Kim and Matsui, 2017; Gillmeier et al., 2018). Simple formulations, such as Rankine's vortex (Rankine, 1872) and Bjerknes-type profiles (Eliassen, 1999), are popular for their mathematical tractability but are limited outside the core region. More advanced three-dimensional representations, including the Sullivan (Sullivan, 1959), Burgers–Rott (Burgers, 1948; Rott, 1958), Vatistas (Vatistas et al., 1991), Kim and Matsui (2017), and Baker–Sterling (Baker and Sterling, 2017) models, introduce explicit dependence on radius and

Peer review under the responsibility of Editorial Board of *Advances in Wind Engineering*.
* Corresponding author.
E-mail address: reda.snaiki@etsmtl.ca (R. Snaiki).

https://doi.org/10.1016/j.awe.2026.100101
Received 12 November 2025; Received in revised form 26 January 2026; Accepted 1 February 2026
Available online 10 February 2026

height and thus capture features beyond the reach of lower-dimensional approaches. For example, the Burgers–Rott solution assumes vertical velocity varies linearly with height, while the Kim–Matsui and Baker–Sterling families parameterize both radial and vertical structure to represent near-surface shear. Despite these advances, analytical models necessarily simplify the physics. Many models effectively reduce the vortex to a single-cell structure with radial inflow and updraft, and their predicted velocity fields vary considerably across parameterizations, making it challenging to establish a universally applicable representation (Kim and Matsui, 2017). Moreover, they struggle to reproduce fine-scale turbulence and complex flow regimes, including transitions to two-cell vortices with a central downdraft, that are routinely observed in laboratory and high-resolution numerical studies (Kim and Matsui, 2017; Gillmeier et al., 2018; Haan et al., 2024).

In addition to analytical formulations, substantial efforts have reproduced tornado vortices and examined their structure through both experimental (Ward, 1972; Church et al., 1979; Refan et al., 2014; Tang et al., 2018; Ashrafi et al., 2021; Zuo et al., 2021) and numerical studies (Lewellen et al., 1997; Natarajan and Hangan, 2012; Gairola and Bitsuamlak, 2019; Zhang et al., 2023b). Laboratory apparatus, typically Ward-type vortex chambers or wind tunnels, generate tornado-like vortices (TLVs) that provide foundational datasets for the field (Ward, 1972; Church et al., 1979; Natarajan and Hangan, 2012). These facilities enable controlled variation of parameters such as swirl ratio and aspect ratio, revealing key structural transitions (e.g., from single-cell to multi-cell vortices) that resemble real tornadoes (Hangan and Kim, 2008; Tang and Zuo, 2018; Wang et al., 2022). Nonetheless, experiments face challenges, including high construction/operation costs, scaling limitations, and difficulty resolving near-surface flow fields, which are the critical regions for assessing tornado-induced damage. Complementing laboratory work, computational fluid dynamics (CFD) has been widely used to reproduce tornado-like vortices with high spatial and temporal resolution and to explore parameter regimes beyond laboratory feasibility (Lewellen et al., 1997; Natarajan and Hangan, 2012; Gairola and Bitsuamlak, 2019; Zhang et al., 2023a). Built on canonical chamber/tunnel configurations, CFD serves as a controllable “numerical laboratory”, enabling systematic studies of how swirl ratio, aspect ratio, and inflow/boundary conditions shape vortex structure. Within CFD, large-eddy simulation (LES) offers higher fidelity by resolving energy-containing eddies while modeling subgrid scales, yielding detailed depictions of tornadic turbulence (Kawaguchi et al., 2019; Satrio et al., 2020; Feng et al., 2022; Rotunno and Bluestein, 2024). LES studies have reproduced the evolution from weak single-cell vortices through vortex breakdown to complex multi-vortex systems, producing high-resolution datasets that often serve as “ground truth” for model development and validation (Chow et al., 2006; Cuxart, 2015; Breton et al., 2017; Rohanizadegan et al., 2023). The principal limitation is computational expense: LES is typically impractical for rapid evaluation across large parameter spaces in engineering design, and results can remain sensitive to subgrid closures and near-surface boundary conditions.

Machine learning (ML) is increasingly used in wind engineering to complement physics-based models (Wu and Snaiki, 2022). Applications span tornado damage assessment and hazard mapping (Sessa and Trapp, 2020; Chen et al., 2021), nowcasting and genesis prediction, severe-weather forecasting, and damage classification (Trafalis et al., 2016; Carani and Pingel, 2023; Zhang et al., 2023c). In tornado-specific studies, convolutional neural networks (CNNs) have been trained on radar imagery and proximity soundings to predict tornado occurrence, while support vector machines (SVMs) and artificial neural networks (ANNs) have been used to detect tornadic signatures in radar-derived velocity fields, improving detection probabilities and reducing false alarms (Trafalis et al., 2016; Lagerquist et al., 2020; Aleskerov et al., 2020; Özgenç et al., 2025). Kernel methods (e.g., SVMs, minimax probability machines) have also shown strong skill for pre-tornadic circulation detection (Trafalis et al., 2006, 2016). Beyond forecasting and detection, ML has been applied to wind-field reconstruction from sparse sensors (Duthé et al., 2023; Rybchuk et al., 2023; Zhong et al., 2023; Huang et al., 2024; Hosseini and Shiri, 2024) and to surrogate modeling of expensive simulations such as LES (Ling et al., 2016; Maulik et al., 2019). Recent progress in physics-informed spatial learning for extreme-weather applications has also emphasized data-efficient inference under scarce and heterogeneous observations, including spatio-temporal GNN formulations for storm-surge forecasting from limited station networks (Jiang et al., 2024) and neural-field approaches that fuse multi-source measurements to reconstruct high-fidelity urban wind profiles (Gu et al., 2026). Complementary advances in wind engineering have further explored deep generative models for imputing missing wind-speed time series under high missingness rates (Liu and Cai, 2025). Among physics-aware approaches, physics-informed neural networks (PINNs) have seen growing use in atmospheric flows, especially at synoptic scales, where they reconstruct tropical-cyclone wind and pressure fields from sparse observations for data assimilation and analysis (Snaiki and Wu, 2019; Eusebi et al., 2024; Hu and Li, 2024); applications to extratropical systems are also emerging within physics-aware weather ML (Snaiki and Wu, 2022). In contrast, tornado-scale applications remain comparatively sparse: recent work shows that PINNs can reconstruct tornado vortices from limited observations with encouraging accuracy (Zhang et al., 2023a), but the setting is far less developed than for larger-scale cyclones. However, PINNs can be challenged by large or irregular domains with sparse data due to the need for dense collocation points and globally enforced constraints, which can limit scalability and robustness in practice. Graph neural networks (GNNs) address several of these limitations by operating directly on irregular, spatially distributed data, scaling to larger domains, and enabling local, edge- or node-level incorporation of physics (Scarselli et al., 2009; Wu et al., 2022). In related applications, GNNs have represented wind/structural response data, predicted tornado-induced building damage, and modeled flow in infrastructure systems (Khodayar and Wang, 2019; Li et al., 2023; Chou et al., 2024; Zhang et al., 2023a; Liu et al., 2025; Zhang et al., 2025). Despite this progress, ML in tornado research has focused mainly on detection, forecasting, and damage classification rather than direct 3-D wind-field reconstruction, motivating hybrid frameworks that integrate data-driven learning with analytical models and high-fidelity CFD datasets for physically consistent yet computationally efficient simulation.

This paper bridges the gap between the efficiency of analytical models and the accuracy of high-fidelity simulations through a hybrid residual-learning framework with two layers of physics guidance. First, an analytical Baker–Sterling baseline provides a physically coherent starting point, embedding core vortex structure. Second, a GNN is trained on LES data to learn residuals in velocity and pressure, with lightweight constraints that encourage mass conservation and momentum balance. These constraints are introduced on a staged schedule, initially prioritizing data fit, then gradually strengthening the physics, to stabilize optimization without over-constraining learning. Predictions are obtained by correcting the analytical baseline with the learned residuals. The approach combines an analytical foundation, graph-based residual learning, and physics-guided regularization and is validated against high-fidelity references. Across a range of swirl ratios and heights, it reduces error relative to the Baker–Sterling baseline while delivering inference times orders of magnitude faster than LES.

2. Methodology

The proposed methodology is a hybrid, two-step framework that combines the strengths of physics-based analytical models and data-driven ML. The core idea is to establish a reliable physical baseline and then develop an ML model to learn and correct its deviations from high-fidelity simulation data. This ensures that the final predictions are not only accurate but also grounded in established physical principles. This section details the acquisition of the ground-truth data, the formulation of the learning problem, and the architecture of the predictive model.

2.1. Data acquisition and preprocessing

The foundation of the proposed data-driven framework is a high-fidelity dataset that accurately represents the complex physics of tornado vortices. For this study, the ground-truth data were derived from published large-eddy simulation (LES) investigations. LES resolves the large, energy-carrying eddies in turbulent flows and is therefore a reliable source of detailed flow-field information for highly unsteady and three-dimensional vortex phenomena. The LES data used here were digitized from the numerical studies of Ishihara et al. (2011) and Liu and Ishihara (2015). Both works employ a numerical Ward-type tornado simulator to generate a range of tornado-like vortices, producing a sufficiently rich set of flow realizations for training and validation.

The selected LES cases span a broad spectrum of vortex structures that are primarily controlled by the swirl ratio (S). The dataset covers the vortex evolution from weak, single-cell structures to more complex behaviors, including vortex breakdown, vortex touchdown, and multi-vortex patterns. In practice, the simulations sample mixed swirl ratios over the range $S = 0.02$ to $S = 2.44$. This range included both single-cell vortices (typically associated with a central updraft) and two-cell vortices (which exhibit a central downdraft), thereby exposing the model to a diverse set of flow physics relevant to engineering applications. From the LES results, the non-dimensional velocity components, tangential (V), radial (U), and vertical (W), together with pressure (expressed via a non-dimensional pressure coefficient C_p or equivalent) are extracted. All quantities are represented as functions of non-dimensional radius and height (e.g., r/r_c, z/r_c) so that the data are consistent across cases and readily comparable. Specifically, the geometric inputs are first expressed in this physically non-dimensional form using the core radius r_c, consistent with both the LES profiles and the analytical baseline definition. Subsequently, the complete set of input features is standardized using training-set statistics (z-score normalization) to improve numerical conditioning during optimization.

A central point of the methodology is to pose the learning problem in terms of a residual field. Rather than asking the neural network to reproduce the full LES field directly, the framework first constructs a physics-based baseline using the analytical Baker–Sterling vortex model (hereafter, the Baker model). The Baker model is a compact, physically grounded representation of a one-cell vortex that captures the primary circulation and characteristic radial inflow and vertical updraft. Because this model necessarily simplifies many aspects of the true flow, the residual R is defined as the difference between the high-fidelity LES field ($\boldsymbol{Y_{LES}}$) and the baseline prediction ($\boldsymbol{Y_{Baker}}$) as $\boldsymbol{R} = \boldsymbol{Y_{LES}} - \boldsymbol{Y_{Baker}}$. By training the ML model to predict $\boldsymbol{R}$, the approach leverages the baseline to encode the large-scale, physically consistent structure of the vortex and reserves the network's capacity for learning the smaller-scale, highly nonlinear corrections (e.g., boundary-layer interactions, secondary flows, and one-cell–to–two-cell transitions) that the analytical model does not capture. To enable learning with a GNN, the raw LES and Baker fields are organized into a graph-compatible representation through a multi-stage preprocessing pipeline. First, the extracted data are grouped into distinct scenarios, each defined by a unique pair (S, z), representing a fixed swirl ratio and a fixed non-dimensional height. Within each scenario, radial samples of the flow variables are collected and interpolated onto a standardized radial grid to obtain a consistent set of radial nodes for every scenario. Where extrapolation is required to reach the chosen grid beyond the measured radial extent, careful extrapolation and, when necessary, controlled clamping are applied to avoid introducing unphysical trends; these safeguards preserve realism in the residual signals used for training.

Finally, each scenario is converted into a small radial graph: nodes correspond to the interpolated radial points, and node features include geometric/physical inputs (for example, r, z, S) together with the Baker baseline fields (the non-dimensional velocity components V, U, and W and pressure P) used for conditioning. Graph edges connect nearest radial neighbors, and edge attributes encode relative geometry via Δr and $|\Delta r|$. Thus, the graph stores both absolute position (through node features) and local spacing (through edge attributes), which helps the GNN learn position-dependent structure while exchanging information with distance-aware messages. The resulting collection of small radial graphs, indexed by (swirl ratio and height), forms the input to the GNN.

2.2. Hybrid modeling approach

The proposed framework is a two-step hybrid system that combines a physics-based analytical baseline with a data-driven, residual-learning graph neural network (GNN). The Baker analytical model provides a compact, physically interpretable baseline that encodes large-scale vortex structure with minimal computation, while the GNN captures the remaining complex, nonlinear corrections required to reproduce high-fidelity large-eddy simulation fields. This hybridization reduces the learning burden on the neural model and improves interpretability and robustness by anchoring predictions to known physics. It should be noted that in this study, 'high-fidelity' denotes agreement with the LES mean radial profiles, rather than prediction of instantaneous turbulent realizations or turbulence statistics. Accordingly, the learned residual represents a mean-field correction to the Baker model that captures systematic structural departures (e.g., two-cell signatures, core-gradient sharpening, and near-ground inflow features) present in the LES mean flow. A schematic of the overall framework is shown in Fig. 1.

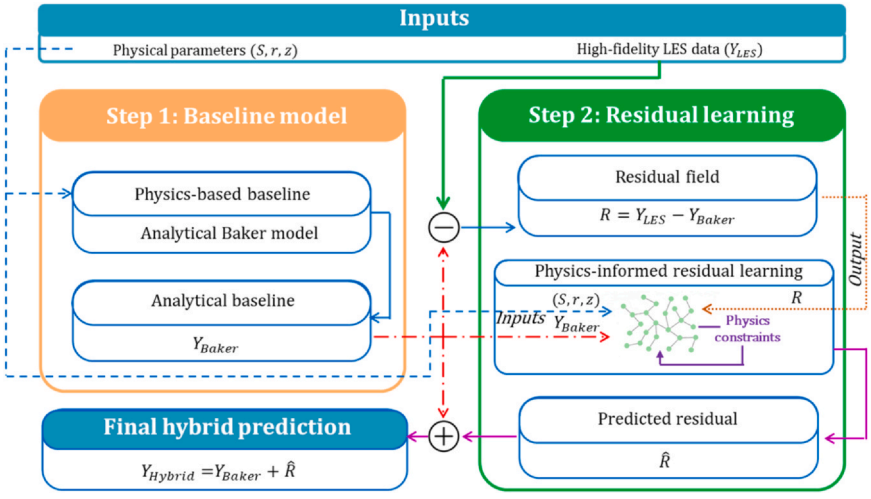

Fig. 1. Schematic representation of the proposed framework.

2.2.1. Step 1: The Baker model baseline

The first step establishes a physical baseline using the Baker model. The Baker model is a simple, well-known analytical representation of a one-cell vortex; it prescribes the dominant tangential circulation together with a radial inflow and an axial updraft profile. In the present framework, the Baker model is evaluated on the same non-dimensional coordinate grid used for the LES data (i.e., the standardized radial nodes at a given height and swirl ratio). The Baker output $\boldsymbol{Y_{Baker}}(r, z; S)$ provides first-order estimates for the flow variables of interest (V, U, W, and P). Using an analytical baseline accomplishes several practical and theoretical goals:

- Reduced learning complexity: By explaining the dominant, large-scale circulation, the Baker model leaves the neural network to learn only the corrective residual field that contains turbulent fluctuations, boundary-layer effects, secondary flows, and structural transitions (e.g., one- to two-cell behavior).
- Physical regularization: The Baker baseline enforces that the learned corrections remain a perturbation about a physically coherent state rather than an unconstrained reconstruction from raw data.
- Computational efficiency: Evaluating the Baker model is negligible compared to LES; combining it with a lightweight GNN yields a practical pipeline suitable for repeated evaluation in engineering workflows.

Formally, for each radial node in a scenario defined by (S, z), the residual target is computed as:

$$\boldsymbol{R}(r, z; S) = \boldsymbol{Y_{LES}}(r, z; S) - \boldsymbol{Y_{Baker}}(r, z; S) \tag{1}$$

and the GNN is trained to predict $\boldsymbol{R}$. The final reconstructed field returned by the hybrid model is simply:

$$\hat{\boldsymbol{Y}}(r, z; S) = \boldsymbol{Y_{Baker}}(r, z; S) + \hat{\boldsymbol{R}}(r, z; S) \tag{2}$$

where $\hat{\boldsymbol{R}}$ is the GNN output.

2.2.2. Step 2: The residual-learning graph neural network

The second step uses a GNN to predict the residual field $\boldsymbol{R}$ on the standardized radial grid for each scenario. A GNN is natural here because the radial profile at fixed (S, z) is spatially structured, and each node's residual depends on neighboring radial states (through gradient-like and nonlinear couplings). The graph formulation explicitly encodes these spatial dependencies, providing a flexible and permutation-invariant computational substrate for message passing.

Each preprocessed scenario (fixed S and z) is converted to a small 1-D radial graph. Specifically, each node in the graph corresponds to an interpolated radial location r_i on the standardized grid. The node features are designed to provide the network with both the physical context and a baseline physics-based estimate. These features include geometric and conditioning inputs $[r_i, z, S]$ augmented by the corresponding velocity and pressure components from the analytical Baker model baseline. In this study, the full node feature vector is:

$$\boldsymbol{x_i} = [r_i, z, S, V_i^{Baker}, U_i^{Baker}, W_i^{Baker}, P_i^{Baker}] \tag{3}$$

where $(V_i^{Baker}, U_i^{Baker}, W_i^{Baker}, P_i^{Baker})$ are the values predicted by the Baker model at the node i. All features are normalized using training-set statistics before being passed to the GNN. The nodes are connected to their K nearest neighbors along the radial axis. Each edge carries simple geometric attributes, such as the signed radial separation $\Delta r = r_j - r_i$ and absolute distance $|\Delta r|$. Edge attributes are provided to the message function so the network can account for nonuniform spacing. The network output at each node is the residual vector $\boldsymbol{R_i} = [R_U, R_V, R_W, R_P]$, which, when added to the Baker baseline, yields the hybrid prediction. It should be noted that the Baker-model outputs are used both to define residual targets and as conditioning features in Eq. (3). While deterministic in (r, z, S), providing them explicitly supplies a physics-informed embedding that helps localize corrections and shifts learning capacity toward LES-specific departures rather than reconstructing the baseline vortex structure from coordinates alone.

The GNN comprises three logical blocks. First, the input encoder, which is a small feedforward network that lifts normalized node features into a latent node embedding. Second, the message-passing layers, where several layers of conditional message passing propagate information between adjacent radial nodes. Each message-passing block aggregates neighbor information (messages computed from pairs of node embeddings and edge attributes) to produce updated node embeddings. Third, the output heads where final MLPs map the node embedding to the residual prediction (predictions are denormalized before physics terms and reporting). A crucial architectural choice is the inclusion of Feature-wise Linear Modulation (FiLM) to condition the message passing on the global swirl ratio S. Concretely, FiLM produces affine modulation parameters $(\gamma(S), \beta(S))$ that scale and shift internal message activations:

$$m' = \gamma(S) \odot m + \beta(S) \tag{4}$$

where m denotes a message vector and $\odot$ denotes elementwise multiplication. FiLM lets a single network adapt its internal processing to different swirl regimes, for example, the relative importance of radial coupling versus local corrections may change as S increases, without training separate models for each S.

The training process minimizes a composite loss that blends data fidelity with physics-based penalty terms. Let $\hat{\boldsymbol{R}}_i$ denote the network residual prediction at node i and let $Y_{Baker,i}$ be the Baker baseline at that node. The data loss is:

$$\mathscr{L}_{data} = \frac{1}{N} \sum_{i=1}^{N} \|\hat{\boldsymbol{R}}_i - \boldsymbol{R}_i^{true}\|^2 \tag{5}$$

where $\boldsymbol{R}_i^{true} = \boldsymbol{Y_{LES,i}} - \boldsymbol{Y_{Baker,i}}$. To promote physical consistency, the total loss adds weighted penalty terms that penalize violations of simplified, relevant governing equations evaluated on the hybrid (Baker + GNN) field. The main penalties used are the continuity equation $\mathscr{L}_{cont}$, the azimuthal momentum equation $\mathscr{L}_\theta$, the radial momentum equation $\mathscr{L}_r$, and the vertical momentum equation $\mathscr{L}_z$. The total loss is the weighted sum:

$$\mathscr{L} = \mathscr{L}_{data} + \lambda_{cont}\mathscr{L}_{cont} + \lambda_\theta \mathscr{L}_\theta + \lambda_r \mathscr{L}_r + \lambda_z \mathscr{L}_z \tag{6}$$

with tunable hyperparameters $\{\lambda_{cont}, \lambda_\theta, \lambda_r, \lambda_z\}$ controlling the relative emphasis of physics penalties. Physics weights are introduced gradually during the early training epochs (two-stage schedule) to stabilize optimization. The spatial derivatives entering Eqs. (5–6) are approximated using finite differences along the ordered radial nodes within each (S, z) profile (the graph connectivity is used for message passing, not for defining differential operators). Central differences are used at interior nodes, one-sided differences are used at the first and last radial nodes, and a small-radius mask is applied in $1/r$ terms to avoid numerical issues near the axis.

All node features and target residuals were standardized using the training-set mean and standard deviation before being passed to the network. Physics-based penalty terms were computed on the predictions after denormalization so that finite-difference gradients and penalty magnitudes retain correct physical units. No vertical-momentum penalty was applied because the available vertical sampling was insufficient to yield robust finite-difference estimates; enforcing a vertical penalty under these conditions would risk introducing noisy or biased constraints. The radial derivatives are approximated with central differences for interior nodes and one-sided differences at boundaries. Points near $r = 0$ are masked to avoid singular $1/r$ terms (or treated with appropriate limits). Weight decay, gradient clipping, and optional dropout are used to stabilize training. At inference, the model outputs the residual $\hat{\boldsymbol{R}}$ for each node; after denormalizing $\hat{\boldsymbol{R}}$, the final hybrid prediction is obtained by adding it to the Baker baseline: $\hat{\boldsymbol{Y}} = \boldsymbol{Y_{Baker}} + \hat{\boldsymbol{R}}$.

The present 1D radial formulation generalizes directly to 2D (r, z) and 3D cylindrical (r, z, θ) graphs by redefining each node as a sample at (r_i, z_j) or (r_i, z_j, θ_k). Graph connectivity can be constructed either (i) by structured local adjacency such as K_r neighbors in r and vertical edges connecting (r_i, z_j) to $(r_i, z_{j\pm1})$, with additional azimuthal edges $(\theta_k \leftrightarrow \theta_{k\pm1})$ when non-axisymmetric structure is modeled, or (ii) by K-nearest neighbors in the chosen coordinate metric (optionally anisotropically scaled to reflect differing resolutions in r, z and θ). Edge attributes are augmented accordingly (e.g., Δr, Δz, $\Delta\theta$, and their magnitudes), while the message-passing update remains unchanged and simply aggregates over the expanded neighborhood. Furthermore, for fixed hidden width and number of message-passing layers, inference cost scales approximately with the number of edges. Consequently, extending from 1D profiles to (r, z) increases computational cost roughly in proportion to the number of vertical levels, and extending to (r, z, θ) increases computational cost roughly in proportion to the number of vertical levels times azimuthal sectors. Despite this increased graph size, surrogate inference remains orders of magnitude cheaper than running a new LES (typically hours to days on HPC), enabling rapid evaluation once training is completed.

The proposed hybrid design confers other advantages. The residual-learning strategy anchored on the Baker baseline reduces sample complexity and improves extrapolation stability near known physics. The GNN enforces locality and permutation invariance while FiLM conditioning on the swirl ratio S allows the same network to adapt across the full family of vortex types represented in the data. Soft physics penalties encourage approximate mass and momentum balance within the training objective, steering the model away from spurious fits that would achieve low data loss but violate fundamental flow constraints. Together, these design choices produce a compact, interpretable hybrid model that attains high fidelity relative to LES at a small fraction of the computational cost. It should be noted that the methodological novelty is not residual learning itself, but a topology-aware residual formulation for tornado wind fields: the correction to the analytical Baker baseline is learned using message passing over a radial graph. In contrast to grid-based residual models, the GNN exploits physically meaningful adjacency and variable node spacing, improving the representation of localized structures (e.g., near-core shear layers) under irregular sampling.

3. Results

This section summarizes the predictive performance of the hybrid PI-GNN framework. First, the aggregate, component-wise quantitative metrics root-mean-square error (RMSE) and mean absolute error (MAE) are reported on the train and test sets, then representative radial profiles and per-case diagnostics are inspected to show how the hybrid PI-GNN corrects the Baker baseline and captures height-dependent physics.

3.1. Model performance and quantitative analysis

The training dataset was constructed by digitizing non-dimensional LES profiles reported by Ishihara et al. (2011) and Liu and Ishihara (2015) spanning swirl ratios $S \in [0.02,\ 2.44]$ and multiple normalized heights z/r_c (approximately 0.1–2.0). The digitized database is stored in tabular form, containing $(r/r_c,\ z/r_c,\ S)$ and the corresponding LES quantities. The digitized LES profiles were mapped onto a common target radial grid using interpolation restricted to the radial support of the available samples for each (S, z) scenario. Specifically, inputs and targets were evaluated only at target-grid nodes lying within the scenario's supported interval, which mitigates boundary artifacts that can occur when profiles are implicitly extended beyond the available data range. Within this supported interval, a shape-preserving Piecewise Cubic Hermite Interpolating Polynomial (PCHIP) was used to reduce overshoot and systematic bias near domain edges, with linear interpolation used as a fallback when PCHIP was unavailable. To improve numerical robustness during optimization, a controlled clamping step was applied after normalization: normalized target values were clipped using a Z-score threshold to limit the influence of rare outliers on gradient updates. This operation acts only on the normalized targets and does not alter the radial coordinate or impose any boundary padding.

With the data prepared, the specific hyperparameters and architectural configurations were standardized as follows. The graph topology was constructed using a K-nearest neighbor algorithm with $k = 4$ in the radial coordinate, where edge features encoded both signed (Δr) and absolute $(|\Delta r|)$ radial distances. The GNN architecture consisted of an MLP encoder mapping inputs to a latent dimension of 128 (Linear–LayerNorm–GELU), followed by 4 message-passing layers of width 128, and a linear output head mapping the latent representation to the four predicted quantities. The framework was implemented in PyTorch and trained using the AdamW optimizer with learning rate of 1×10^{-3} and weight decay of 1×10^{-4}. A ReduceLROnPlateau scheduler was applied (factor 0.5, patience 200 epochs, minimum learning rate 10^{-6}). Each optimization step processes one complete scenario graph (one radial-profile graph), with scenarios randomly shuffled each epoch. Models were trained for 3000 epochs, and the reported checkpoint corresponds to the minimum training objective over epochs. A fixed global random seed was used for deterministic initialization and reproducible data splitting. A staged physics-penalty schedule was applied: the global physics weight was held at zero for the first 500 epochs (warm-up), then linearly increased over the subsequent 1000 epochs to a maximum scaling factor of $\lambda_{\max} = 0.05$, and held constant thereafter. The weighting coefficients for the governing-equation penalties were fixed at $\lambda_{cont} = 2 \times 10^{-3}$ for continuity and $\lambda_r = \lambda_\theta = 5 \times 10^{-4}$ for the azimuthal and radial momentum terms, respectively. This global scaling factor ($\lambda_{\max} = 0.05$) was selected based on a sensitivity analysis, which identified it as the optimal trade-off, reducing RMSE by approximately 37% compared to the baseline ($\lambda_{\max} = 0$) while avoiding the over-smoothing observed at higher weights ($\lambda_{\max} \geq 0.10$). Input coordinates are expressed in non-dimensional form $(r/r_c,\ z/r_c)$ along with swirl ratio S; for hybrid variants, the analytical baseline fields were concatenated to form a 7-dimensional feature vector. The network outputs four components, and all inputs/outputs were standardized via Z-score normalization using training-set statistics.

With this configuration established, Table 1 reports the RMSE and MAE for each of the four modeled fields (normalized tangential velocity V/V_c, radial velocity U/V_c, vertical velocity W/V_c, and nondimensional pressure $P/\rho V_c^2$) on the training and test sets for both the analytical Baker baseline and the proposed hybrid PI-GNN.

Overall, the proposed model achieves substantially lower errors across all components. On the test set, the Baker baseline yields a global RMSE of 0.8384 and MAE of 0.4554, whereas the hybrid PI-GNN reduces these to 0.0039 and 0.0025, respectively, corresponding to an overall RMSE reduction of 99.5% relative to the analytical baseline. Component-wise, the hybrid PI-GNN attains test RMSE/MAE values of 0.0027/0.0020 for V/V_c, 0.0015/0.0010 for U/V_c, 0.0029/0.0021 for W/V_c, and 0.0066/0.0050 for $P/\rho V_c^2$, consistently outperforming the Baker model in each field.

Table 1
Component-wise summary (train/test).

Component	Set	$\text{RMSE}_{\text{Baker}}$	$\text{MAE}_{\text{Baker}}$	RMSE_{GNN}	MAE_{GNN}
V/V_c	Train	0.6424	0.5280	0.0034	0.0024
	Test	0.6300	0.5161	0.0027	0.0020
U/V_c	Train	0.5181	0.4149	0.0017	0.0012
	Test	0.5303	0.4395	0.0015	0.0010
W/V_c	Train	0.5005	0.3072	0.0026	0.0019
	Test	0.4258	0.2803	0.0029	0.0021
$P/\rho V_c^2$	Train	1.3977	0.5819	0.0063	0.0047
	Test	1.3972	0.5858	0.0066	0.0050

An additional ablation was conducted to quantify the impact of residual learning around the analytical baseline. Specifically, the proposed hybrid PI-GNN (residual over Baker) was compared against a full-field GNN trained to predict the LES fields directly (i.e., identical graph construction and training protocol, but without using the Baker model in either the target definition or the input features). On the held-out test set, both variants deliver very similar accuracy: the hybrid PI-GNN model achieves an aggregate RMSE of 0.0039 (MAE = 0.0025), while the full-field GNN attains an RMSE on the order of 4×10^{-3} (and MAE on the order of 3×10^{-3}). Peak-based indicators follow the same trend, with both approaches producing comparable errors in the peak tangential velocity magnitude and its radial location. These results indicate that the dominant performance gains arise from the graph-based spatial inductive bias (and physics regularization when enabled), while the Baker-based residual formulation provides a physically interpretable decomposition without materially changing predictive accuracy on this dataset. From a practical standpoint, incorporating the Baker baseline remains advantageous in data-scarce regimes because it supplies a physically plausible reference field that reduces the learning burden and stabilizes predictions when observations are sparse, unevenly sampled, or partially missing.

The influence of physics regularization was also examined by enabling/disabling the governing-equation penalty terms while keeping the architecture and data split fixed. Across both the residual Hybrid formulation and the full-field GNN variant, the aggregate RMSE/MAE on the present benchmark changes only marginally when physics is enabled, with the test-set error degrading by less than ~5% in the absence of physics constraints. This indicates that the supervised LES signal is sufficient to learn a good mapping under the current sampling density. In this setting, the primary role of the physics penalty is better interpreted as a consistency and robustness prior: it discourages violations of radial continuity and momentum balance and reduces the likelihood of physically implausible solutions in low-support regimes (e.g., sparser or noisier profiles), even when improvements in global error metrics are necessarily limited.

To rigorously evaluate the proposed hybrid PI-GNN, performance was benchmarked against two representative machine-learning baselines: a standard Multilayer Perceptron (MLP) and a one-dimensional Convolutional Neural Network (1D-CNN). All learning-based models were trained and evaluated using the same data splits, identical input/output normalization, and a matched training budget (same optimizer family and comparable tuning effort) to ensure a fair comparison. The MLP baseline learns the residual correction using fully connected layers and treats each radial location independently, providing an ablation that removes explicit neighborhood modeling. The 1D-CNN baseline treats each radial wind profile as an ordered sequence on the target grid and applies convolutional filters along the radial direction, representing a standard gridded approach for one-dimensional profiles. Table 2 summarizes the comparison using aggregate RMSE and MAE. As reported in Table 2, the hybrid PI-GNN achieves the lowest error among all learned models (RMSE = 0.0039), improving over the residual MLP (RMSE = 0.0055) and the 1D-CNN (RMSE = 0.0124). This indicates that incorporating graph-based neighborhood structure yields measurable benefit beyond pointwise regression (MLP) and standard sequence convolutions (CNN) for this problem setting, particularly when profiles have scenario-dependent radial support and the mapping depends on (S, z) in addition to r/r_c.

Beyond predictive accuracy, the proposed framework offers a computational speedup of several orders of magnitude relative to the numerical source. The Hybrid PI-GNN was trained on a standard CPU for 3000 epochs, requiring a total wall-clock time of approximately 11 min (674 s). Once trained, the model acts as a near-instantaneous surrogate, performing inference in approximately 3.32 ms per query. This effectively transforms the high-cost fluid dynamics problem ($10^2 - 10^3$ CPU-hours for LES) into a rapid function evaluation, enabling parametric sweeps that would be prohibitive using direct CFD. Finally, given that the training data were derived from digitized LES flow fields, a robustness analysis was conducted to quantify sensitivity to potential input uncertainty or measurement errors. Zero-mean Gaussian noise was injected into the input features across noise levels ranging from 0% to 10% to evaluate predictive stability. The results indicate that the hybrid architecture remains robust under increasing uncertainty. Under baseline conditions (0% noise), the model achieved an RMSE of 0.0038. As noise levels increased to 1%, 2%, and 5%, the RMSE rose to 0.0078, 0.0136, and 0.0336, respectively. Even under substantial perturbation (10% noise), the error remained bounded at 0.0733. The monotonic increase in error suggests that performance degradation is controlled and linear, confirming that the hybrid formulation is numerically stable and does not exhibit brittle failure modes under plausible measurement perturbations.

Table 2
Performance comparison against alternative ML architectures.

Model Architecture	Hybrid GNN	Standard MLP	1D-CNN
RMSE (Test)	0.0039	0.0055	0.0124
MAE (Test)	0.0025	0.0037	0.0092

3.2. Case studies

To highlight where the hybrid PI-GNN provides the most meaningful improvements beyond the analytical baseline, radial profiles are examined for a representative moderate-swirl case ($S = 0.31$), which acts as a standard benchmark used in structural engineering literature. Fig. 2 compares predictions against LES at four heights ($z/r_c \approx 0.2,\ 0.5,\ 1.0,\ 2.0$), thereby capturing the vertical evolution of the wind and pressure fields. In the near-ground region ($z/r_c \approx 0.2$ and 0.5), where boundary-layer effects and corner-flow interactions are most pronounced, the Baker model exhibits systematic bias, most notably in the radial inflow component U and in the near-core pressure deficit. The hybrid PI-GNN corrects these departures and brings the profiles into close agreement with the LES reference while maintaining smooth, physically plausible gradients. At higher elevations ($z/r_c \approx 1.0$ and 2.0), the vortex core broadens and the outer-flow decay becomes increasingly important; in this regime, the hybrid model continues to track the evolving structure and mitigates the baseline's tendency to misrepresent the tangential velocity V decay in the outer region. Collectively, these profiles demonstrate that the hybrid formulation consistently compensates for structural limitations of the analytical prior across heights, while preserving physically coherent radial trends required for engineering use.

Quantitative analysis of these profiles confirms the precision of the method. For the critical near-ground case ($z/r_c \approx 0.2$), the hybrid PI-GNN reduces the tangential velocity RMSE from 0.1852 (Baker baseline) to 0.0026 (Hybrid), a reduction of over 98%. Crucially, the model accurately recovers the vortex core structure, which is essential for determining peak wind loads. As shown in the validation metrics, the hybrid model matches the LES peak velocity magnitude (V_{max}) with good precision, yielding a discrepancy of only $0.0008V_c$ at $z/r_c \approx 0.2$ and $0.0017V_c$ at $z/r_c \approx 2.0$. Furthermore, the radius of maximum wind (r_{max}) is identified within $0.1r_c$ across all heights (e.g., predicting $r_{max} = 1.3$ versus observed 1.2 at $z/r_c \approx 0.2$). This deviation corresponds to the spatial resolution of the sampling grid, indicating that the model has effectively converged to the limit of the data density.

To assess the model's robustness under more challenging flow topologies, the evaluation was extended to high-swirl regimes where the vortex structure undergoes fundamental changes. Figs. 3 and 4 present the radial profiles for an elevated swirl ratio ($S = 0.65$) and a very high swirl ratio ($S = 2.44$), respectively. Fig. 3 ($S = 0.65$) illustrates a transitional regime. While the analytical Baker–Sterling model captures the general Rankine-like shape of the tangential velocity, it struggles to resolve the core broadening and the exact magnitude of the pressure deficit. The hybrid PI-GNN effectively corrects these deviations, maintaining a low RMSE of 0.003–0.004

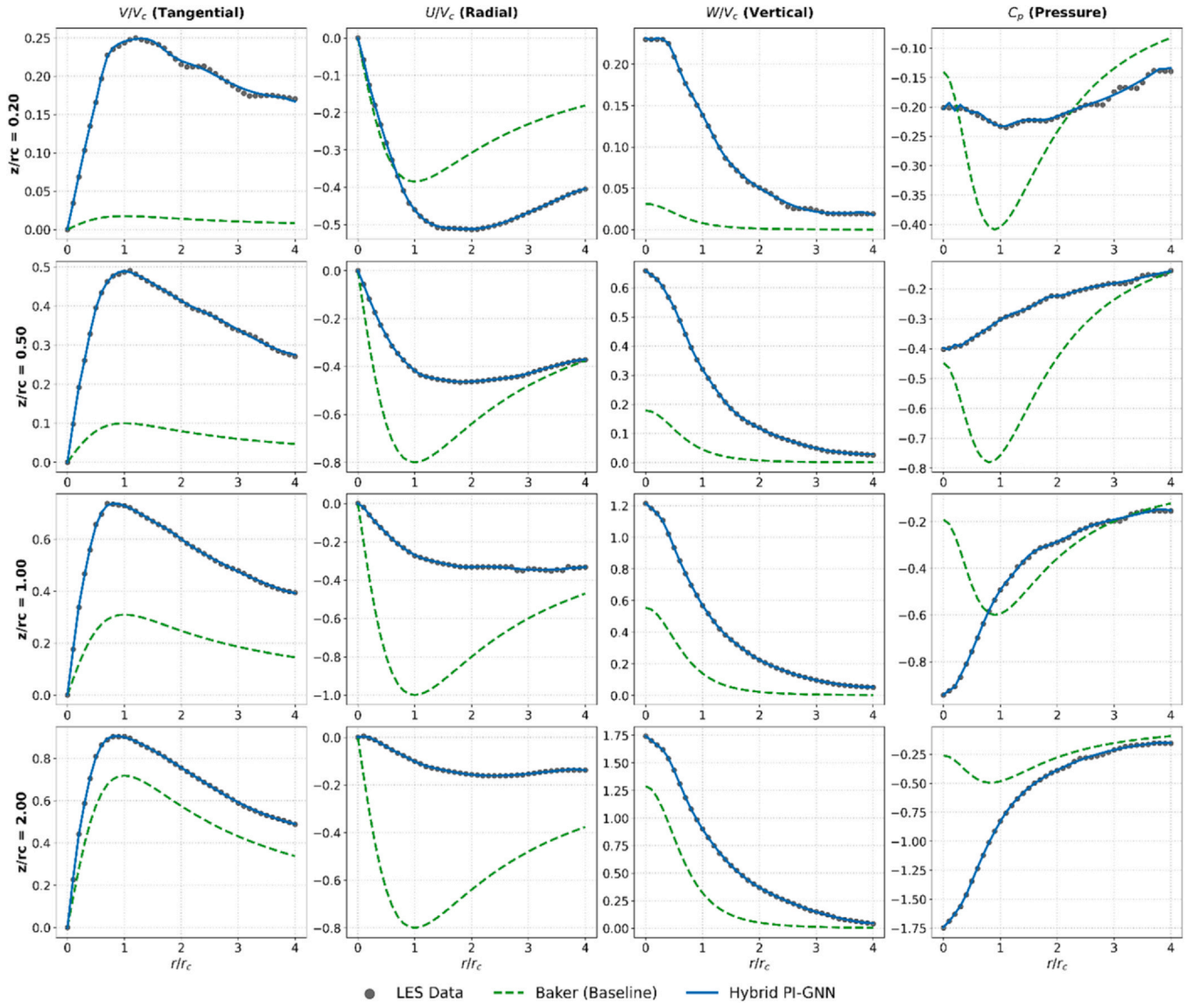

Fig. 2. Vertical evolution of the vortex structure for a moderate swirl ratio ($S = 0.31$). Comparisons show the LES ground truth (black symbols), the analytical Baker baseline (green dashed lines), and the hybrid PI-GNN (blue solid lines) at four elevations ($z/r_c \approx 0.2,\ 0.5,\ 1.0,\ 2.0$). Columns display normalized tangential, radial, and vertical velocities, and pressure coefficient.

across heights. Quantitative analysis confirms that the model captures the structural evolution perfectly: it tracks the expansion of the radius of maximum wind from $0.5r_c$ at $z/r_c = 0.2$ to $1.\ 4r_c$ at $z/r_c = 1.0$ with zero deviation from the LES grid. Notably, in the vertical velocity component (W/V_c), the hybrid model begins to capture the flattening of the central updraft, a precursor to vortex breakdown that the analytical baseline fails to represent.

To assess the model's robustness under challenging flow topologies, the evaluation was extended to a high-swirl regime ($S = 2.44$) where the vortex structure typically undergoes breakdown. Fig. 4 presents the radial profiles for tangential velocity (V/V_c) and pressure coefficient at three distinct elevations ($z/r_c \approx 0.1,\ 0.4,\ 1.0$). In this regime, the strong centrifugal forces distort the vortex core, a feature that the analytical Baker–Sterling model struggles to parameterize accurately. As shown in the top row of Fig. 4, the analytical baseline frequently misplaces the radius of maximum wind ($r_{\max}$) and underestimates the peak magnitude in the near-ground region ($z/r_c = 0.1$). The hybrid PI-GNN effectively corrects these structural deviations, aligning closely with the LES peak velocities; at $z/r_c = 0.1$, the model predicts a peak velocity of $1.335V_c$, virtually identical to the LES benchmark of $1.344V_c$. Similarly, the pressure recovery (bottom row) is significantly improved (RMSE ≈ 0.007). The analytical model fails to capture the extreme pressure deficits observed in the core, which are critical for structural loading calculations, while the hybrid model restores the correct pressure minimum, aligning closely with the deep suction peaks in the LES data.

It is also worth noting that while not explicitly presented in Fig. 4, the hybrid PI-GNN demonstrates similar robustness in the radial and vertical velocity components. Specifically, at this high swirl ratio ($S = 2.44$), the vortex enters a two-cell regime characterized by a central downdraft. While the analytical baseline erroneously predicts a consistent updraft, the hybrid model successfully captures the sign reversal in the core vertical velocity, confirming that the residual learning framework can correct topological errors in the flow structure even when the analytical prior is qualitatively distinct.

4. Discussion

The results demonstrate the efficacy of the proposed hybrid modeling framework: by combining a simple physics-based predictor with a GNN that learns residual corrections, the method attains high fidelity for velocity and pressure profiles while remaining computationally

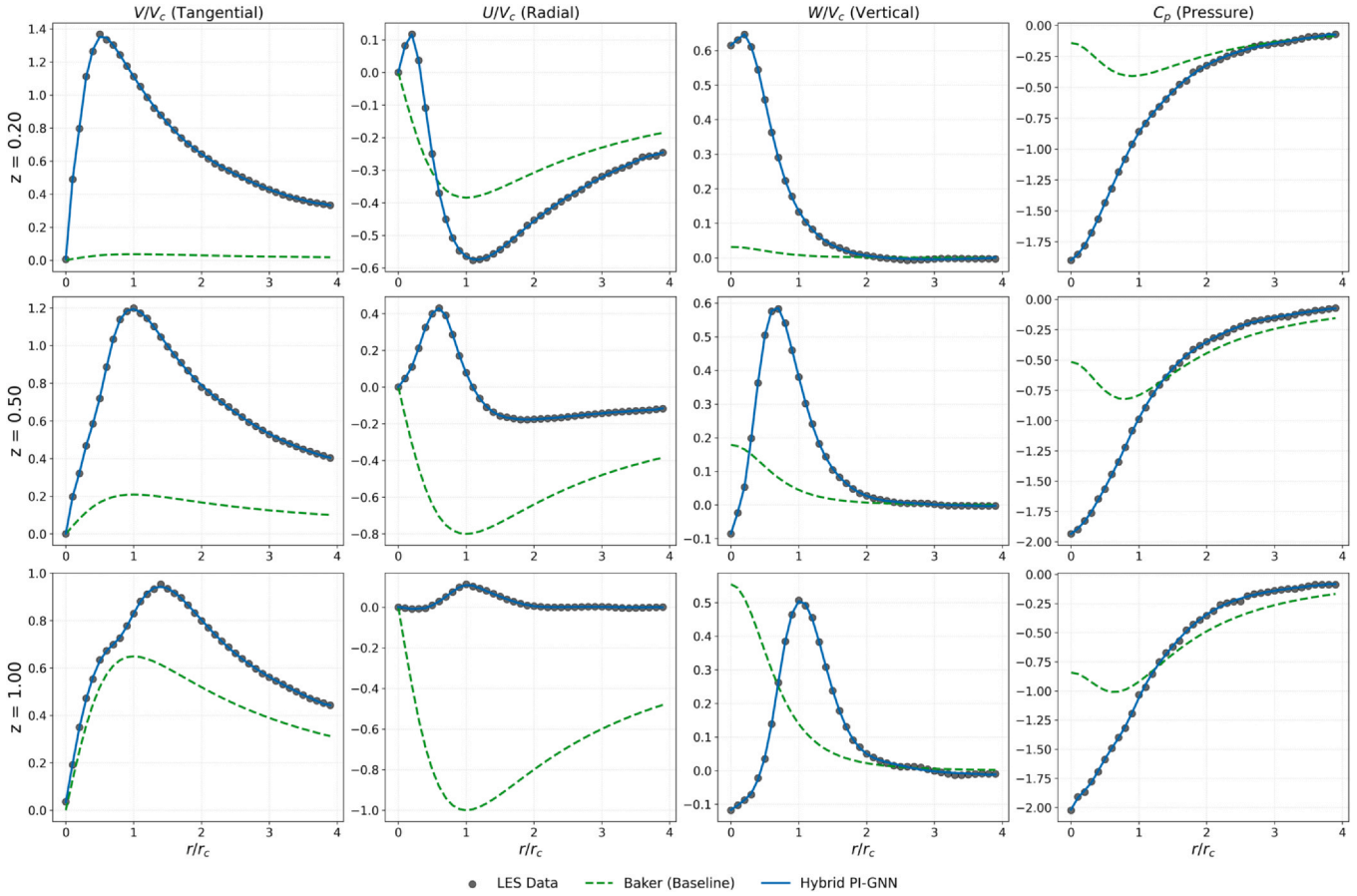

Fig. 3. Prediction results for the elevated swirl case ($S = 0.65$). The hybrid PI-GNN (blue) refines the core radius and peak magnitude predictions of the analytical baseline (green), particularly in the radial (U) and vertical (W) velocity components where the transition to a broader core structure is evident.

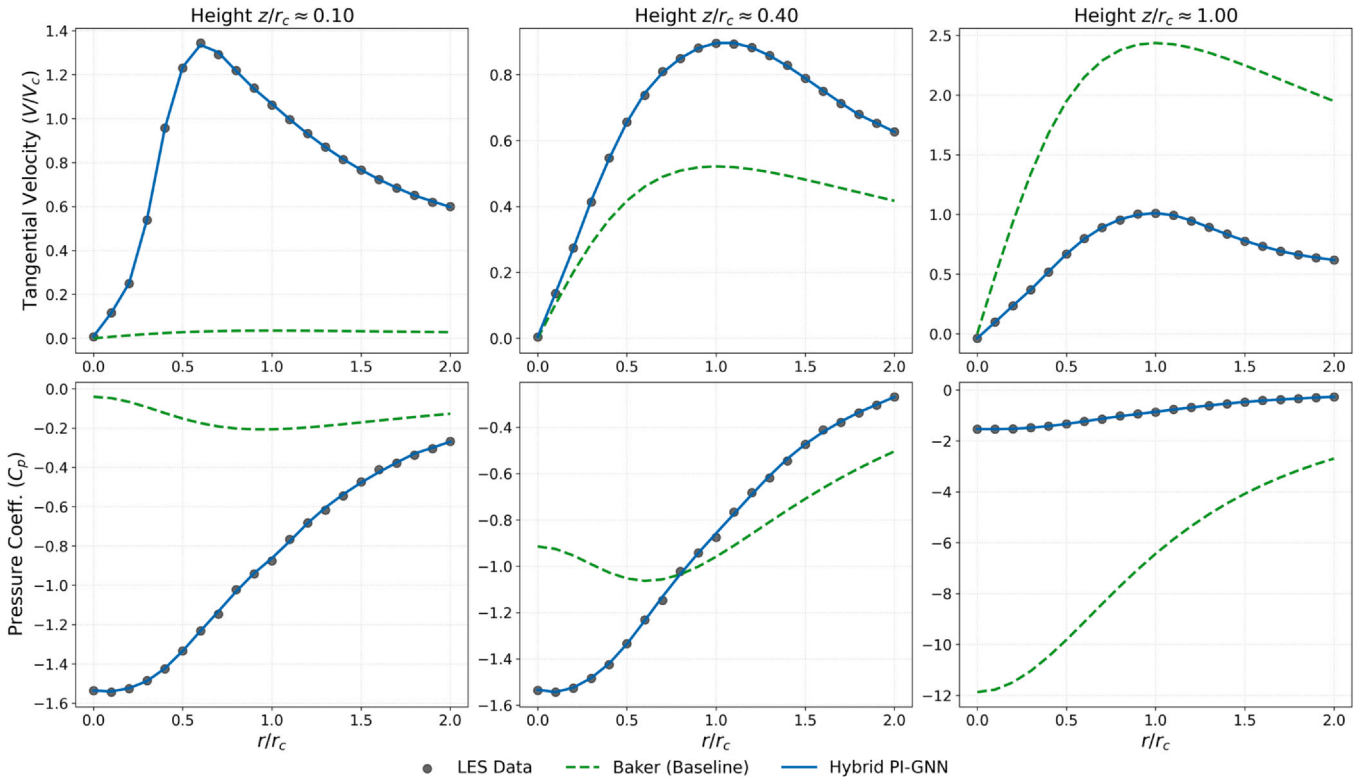

Fig. 4. Prediction results for the high-swirl case ($S = 2.44$) at three elevations ($z/r_c \approx 0.1,\ 0.4,\ 1.0$). The top row displays tangential velocity and the bottom row displays pressure coefficient.

inexpensive. The following sections interpret these findings, highlight the significance of the hybrid physics-informed approach, and outline implications and future directions for tornado modeling and wind-engineering applications.

4.1. Interpretation of model performance

The hybrid PI-GNN substantially outperforms the Baker baseline because of two complementary capabilities. First, the analytical model supplies a compact, physically meaningful approximation of the mean vortex field; second, the hybrid PI-GNN focuses its representational power on the remaining complex, non-linear structure by learning the residual (LES minus baseline). This residual formulation simplifies the learning task because, rather than reconstructing the entire flow, the network concentrates on higher-order, height-dependent physics that the analytical approximation neglects. Concretely, the model recovers near-surface intensification of tangential velocity, captures the structural transition from single-cell to two-cell vortices (including central downdrafts), and restores localized radial inflow and sharp near-core pressure gradients that the baseline systematically under- or over-predicts. These improvements are reflected not only in reduced aggregate errors but also in peak-based engineering quantities, including the maximum tangential velocity and its radial location.

Because the Baker model is inviscid, it does not represent frictional near-ground effects. In the proposed hybrid formulation, these effects are captured indirectly through the learned residual, which is trained to match the LES mean profiles. In the lowest resolved layers available in the dataset (approximately $z/r_c \approx 0.1 - 0.2$), the hybrid predictions exhibit systematic departures from the Baker reference that are consistent with ground-friction influence in LES, including reduced tangential velocity magnitude and intensified radial inflow relative to the inviscid baseline.

Overall, the proposed hybrid model reproduces the LES profiles with consistently high accuracy across heights and swirl ratios, and the remaining mismatches are small in magnitude. As is typical for profile reconstruction problems, the residual discrepancies are not systematic across the domain; instead, they are localized to the most challenging flow regions where gradients and curvature are largest. These localized errors occur primarily near the core/shear-layer $r \approx r_c$ and in the lowest resolved layers, where corner-flow dynamics intensify near-ground shear and modify the inner-core structure. Outside these high-gradient zones, the predicted profiles remain in close agreement with LES over the supported radial range.

The second key ingredient is the incorporation of physics-based penalty terms in training. These soft constraints, derived from continuity and momentum balances, bias the optimization toward physically plausible solutions and discourage fits that achieve low data error while violating basic fluid-dynamic relationships. In practice, the penalties improve stability and robustness while preserving the flexibility needed to correct systematic baseline deficiencies. Together, residual learning and physics-guided regularization yield predictions that are both accurate and physically consistent within the scope of the available data.

4.2. Significance and modularity of the hybrid model

This study highlights the potential of hybrid modeling in scientific domains. The two-stage architecture, an inexpensive analytical predictor followed by a data-driven corrector, retains the interpretability and domain knowledge of classical models while leveraging the approximation capacity of GNNs to capture missing physics. An important advantage is modularity: although the Baker model is used as a convenient reference, the formulation is not inherently tied to that choice and applies equally to other differentiable analytical vortex baselines through the same additive decomposition $\boldsymbol{Y_{total} = Y_{baseline} + Y_{residual}}$. In this sense, substituting the baseline does not alter the learning pipeline, graph construction, or physics-regularized optimization; rather, it primarily changes the structure and magnitude of the residual field that must be learned. For example, simpler parametric profiles (e.g., Rankine-type formulations) tend to induce larger, lower-frequency residual components that encode more of the mean vortex organization (including core-transition behavior), whereas more expressive baselines reduce the residual amplitude and shift the learning burden toward higher-order LES-specific departures from the parametric form. This provides a practical mechanism for improving data efficiency by selecting a baseline that reduces dominant systematic bias in the target regime. Architectural modularity is beneficial as well: while the proposed model does not employ attention or Fourier features, such components can be integrated as drop-in substitutes without changing the physics-guided training protocol. More generally, the residual strategy reduces the amount of training data required to achieve a given accuracy and improves robustness across a range of swirl ratios and heights. The graph-based design is especially well suited here: by operating on radial nodes and explicit radial neighborhoods, the GNN encodes spatial coupling and adapts to swirl-dependent variations in vortex structure, allowing a single learned model to cover multiple regimes, from one-cell and two-cell vortices to near-surface intensification, without per-case reengineering. Although the Baker baseline represents a one-cell reference vortex, the hybrid prediction is not constrained to remain one-cell because the learned component adds a data-driven correction to the baseline field. Two-cell behavior is expressed through a structured residual that introduces the additional profile features present in LES, such as a secondary extremum and/or sign reversal in the vertical velocity, with consistent adjustments in the radial and tangential components. Consequently, the reported 'transition' reflects how the residual contribution evolves with (S, z): it remains small when the one-cell baseline is adequate and becomes more structured when two-cell signatures emerge in the data.

4.3. Implications, limitations, and future outlook

The hybrid model has direct implications for wind engineering. Because it generates high-fidelity wind and pressure fields orders of magnitude faster than LES, it enables rapid scenario screening, more extensive probabilistic structural-response sampling, and better-informed design guidance for tornado-resistant systems. Accurate near-ground velocity and pressure predictions are particularly valuable for estimating structural loads and for designing mitigation measures. Several caveats and opportunities remain. First, the present model is trained on idealized LES data; robustness in operational settings requires evaluation. Moreover, the framework is trained on non-dimensional profiles (e.g., velocities normalized by a characteristic velocity scale and spatial coordinates normalized by the core radius), such that the learned residual mapping is expressed in similarity variables rather than in dimensional form. However, Reynolds-number effects are not explicitly parameterized in the current conditioning inputs. Consequently, direct extrapolation of the learned residuals across Reynolds' regimes cannot be asserted, and applicability to full-scale tornado conditions should be interpreted in relation to the degree of Reynolds-number similarity exhibited by the corresponding non-dimensional mean profiles. A practical pathway to strengthen scale robustness is to augment the conditioning space with regime descriptors (e.g., Reynolds number, surface-roughness/friction parameters, or translation/boundary-layer indicators) and to apply transfer learning or domain adaptation using complementary datasets (e.g., mobile radar retrievals, wind-tunnel measurements, or LES ensembles spanning roughness and translation effects). In this direction, the graph formulation is naturally suited to multi-source, irregular observations because measurements can be represented directly as graph nodes with heterogeneous feature embeddings, avoiding interpolation onto a fixed Cartesian grid and preserving the native sampling geometry. A practical workflow is to pre-train the model on larger LES ensembles to learn

general vortex structure and then fine-tune on smaller, noisier observational datasets to improve realism and calibration; related domain-adaptation strategies (e.g., feature-space alignment or adversarial objectives) can mitigate simulation-to-observation distribution shifts while retaining the physics-regularized inductive bias of the hybrid formulation.

Second, the physics terms are implemented as soft constraints and their relative weighting requires tuning; systematic studies of sensitivity, alternative formulations (e.g., augmented-Lagrangian schemes, hard constraints), and ablations for the modified architecture are warranted. The current physics-based regularization is evaluated using finite differences in the radial coordinate only and are applied independently to each (S, z) profile. Because vertical gradients are not reliably resolved with the available sampling, terms involving $\partial(.)/\partial z$ and fully coupled three-dimensional conservation are not enforced. Accordingly, the physics loss is interpreted as a partial, profile-level radial regularization: it promotes radial continuity consistency and a cyclostrophic-style radial momentum balance under an axisymmetric assumption within each height layer, rather than constituting a full Navier–Stokes constraint. In this sense, the penalties provide a physically motivated inductive bias that stabilizes learning and encourages plausible radial profile structure, while complete 3D physical consistency remains outside the scope of the present dataset. With higher vertical-resolution datasets, vertical connectivity can be introduced by linking (r, z) nodes to $(r, z \pm \Delta z)$, enabling $\partial(.)/\partial z$ operators to be computed along vertical edges and allowing a vertical momentum-balance penalty to be incorporated into the physics loss. In the present dataset, the absence of an explicit vertical-momentum constraint implies that near-surface vertical structure is primarily data-driven; therefore, W predictions in the lowest layers may be less physically constrained than the tangential and radial components, and this should be considered when interpreting engineering-relevant near-ground estimates.

Third, with sufficient data coverage, the graph representation can be extended from 1-D radial chains to 2-D $r - z$ graphs, enabling message passing across both radial and vertical neighbors and improving the modeling of shear layers and height-dependent structure; physics penalties would naturally generalize to 2-D divergence and momentum balances. In regimes with non-axisymmetric features or multi-vortex states, a full 3-D cylindrical graph (adding azimuthal connectivity) becomes attractive, provided volumetric LES or laboratory measurements are available. Although such extensions are technically straightforward, the dominant bottleneck is data acquisition: training and validating higher-dimensional models requires volumetric reference fields with sufficient resolution and coverage to support reliable gradients and neighborhood connectivity in three dimensions. Compared to the sparse radial profiles used here, generating and storing 3-D LES datasets entails substantially higher computational cost, simulation time, and post-processing/storage overhead, which may limit data availability in the near term.

Finally, given the framework's modularity, performance can be improved further by adopting different analytical baselines or ensemble/multi-model strategies; choosing a baseline that reduces dominant systematic bias in a given regime lowers residual complexity and typically improves data efficiency and final accuracy.

5. Conclusion

This study introduced and validated a hybrid, physics-informed machine-learning framework for high-fidelity modeling of tornado wind fields. The approach addresses the trade-off between the computational efficiency of analytical models and the accuracy of large-eddy simulations (LES). Using a two-step process, an analytical Baker baseline followed by a residual-learning graph neural network (GNN), the framework achieves substantial accuracy gains over the standalone analytical model and closely approximates LES fields at a fraction of the computational cost. The GNN is conditioned on global vortex parameters such as the swirl ratio and is trained with soft physics constraints that encourage mass and momentum consistency, enabling it to capture complex, non-linear flow features, including transitions between one-cell and two-cell vortices that analytical formulations often simplify. The primary contribution lies in the residual-learning methodology anchored to a physically interpretable baseline. This modular design is general and can be paired with alternative analytical or empirical vortex models to reduce residual complexity, improve data efficiency, and enhance final accuracy. Overall, the framework provides a computationally tractable pathway for producing high-fidelity wind and pressure fields for engineering applications, supporting faster scenario screening, improved risk assessment, and more informed wind-resistant design. This hybrid modeling paradigm offers a promising direction for computational wind engineering and related scientific domains where combining domain knowledge with data-driven methods is essential for tackling complex flows.

CRediT authorship contribution statement

Reda Snaiki: Writing – review & editing, Writing – original draft, Visualization, Validation, Supervision, Software, Resources, Project administration, Methodology, Investigation, Funding acquisition, Formal analysis, Conceptualization. **Seyedeh Fatemeh Mirfakhar:** Writing – review & editing, Methodology, Investigation, Formal analysis, Data curation.

Data availability

The data that supports the findings of this study are available from the corresponding author upon reasonable request.

Declaration of Competing Interest

Reda Snaiki is an editorial board member for *Advances in Wind Engineering*, and he was not involved in the editorial review or the decision to publish this article. The authors declare that they have no other known competing financial interests or personal relationships that could have appeared to influence the work reported in this paper.

Acknowledgment

This work was supported by the Natural Sciences and Engineering Research Council of Canada (NSERC) [grant number CRSNG RGPIN 2022–03492].

References

Aleskerov, F., Demin, S., Richman, M.B., Shvydun, S., Trafalis, T.B., Yakuba, V., 2020. Constructing an efficient machine learning model for tornado prediction. International Journal of Information Technology Decision Making 19, 1177–1187. https://doi.org/10.1142/s0219622020500261

Ashrafi, A., Romanic, D., Kassab, A., Hangan, H., Ezami, N., 2021. Experimental investigation of large-scale tornado-like vortices. Journal of Wind Engineering and Industrial Aerodynamics 208, 104449. https://doi.org/10.1016/j.jweia.2020.104449

Baker, C.J., Sterling, M., 2017. Modelling wind fields and debris flight in tornadoes. Journal of Wind Engineering and Industrial Aerodynamics 168, 312–321. https://doi.org/10.1016/j.jweia.2017.06.017

Breton, S.P., Sumner, J., Sørensen, J.N., Hansen, K.S., Sarmast, S., Ivanell, S., 2017. A survey of modelling methods for high-fidelity wind farm simulations using large eddy simulation. Philosophical Transactions of the Royal Society A Mathematical Physical and Engineering Sciences 375, 20160097. https://doi.org/10.1098/rsta.2016.0097

Burgers, J.M., 1948. A mathematical model illustrating the theory of turbulence. Advances in Applied Mechanics 1, 171–199. https://doi.org/10.1016/s0065-2156(08)70100-5

Cao, Y.W., Liu, Z.Q., 2023. Study of wandering motion effects on the tornado-borne debris using proposed simplified numerical models. Journal of Wind Engineering and Industrial Aerodynamics 233, 105318. https://doi.org/10.1016/j.jweia.2023.105318

Carani, S., Pingel, T.J., 2023. Detection of Tornado damage in forested regions via convolutional neural networks and uncrewed aerial system photogrammetry. Natural Hazards 119, 143–166. https://doi.org/10.1007/s11069-023-06125-4

Chen, Z.A., Wagner, M., Das, J., Doe, R.K., Cerveny, R.S., 2021. Data-driven approaches for tornado damage estimation with unpiloted aerial systems. Remote Sensing 13, 1669. https://doi.org/10.3390/rs13091669

Chou, Y.T., Chang, W.T., Jean, J.G., Chang, K.H., Huang, Y.N., Chen, C.S., 2024. StructGNN: An efficient graph neural network framework for static structural analysis. Computers Structures 299, 107385. https://doi.org/10.1016/j.compstruc.2024.107385

Chow, F.K., Weigel, A.P., Street, R.L., Rotach, M.W., Xue, M., 2006. High-resolution large-eddy simulations of flow in a steep Alpine valley. Part I: Methodology, verification, and sensitivity experiments. Journal of Applied Meteorology and Climatology 45, 63–86. https://doi.org/10.1175/JAM2322.1

Church, C.R., Snow, J.T., Baker, G.L., Agee, E.M., 1979. Characteristics of tornado-like vortices as a function of swirl ratio: A laboratory investigation. Journal of the Atmospheric Sciences 36, 1755–1776. https://doi.org/10.1175/1520-0469(1979)036<1755:cotlva>2.0.co;2

Cuxart, J., 2015. When can a high-resolution simulation over complex terrain be called LES? Frontiers in Earth Science 3, 87. https://doi.org/10.3389/feart.2015.00087

Davies-Jones, R., 2015. A review of supercell and tornado dynamics. Atmospheric Research 274–291. https://doi.org/10.1016/j.atmosres.2014.04.007

Dong, X., Zhao, L., Chen, X., Huang, S.K., Chen, M., 2025. Tornado-induced load distribution patterns and structural effects of a super large cooling tower. Journal of Fluids and Structures 133, 104275. https://doi.org/10.1016/j.jfluidstructs.2025.104275

Duthé, G., Abdallah, I., Barber, S., Chatzi, E., 2023. Graph neural networks for aerodynamic flow reconstruction from sparse sensing. arXiv 2301, 03228. https://arxiv.org/abs/2301.03228.

Eliassen, A., 1999. Vilhelm Bjerknes's early studies of atmospheric motions and their connection with the cyclone model of the Bergen School. In: Shapiro, M.A., Grønås, S. (Eds.), The life cycles of extratropical cyclones. American Meteorological Society, pp. 5–13.

Eusebi, R., Vecchi, G.A., Lai, C.Y., Tong, M.J., 2024. Realistic tropical cyclone wind and pressure fields can be reconstructed from sparse data using deep learning. Communications Earth Environment 5, 8. https://doi.org/10.1038/s43247-023-01144-2

Feng, Y., Hao, J.M., Han, W.S., Su, Q.K., Wu, T., 2022. An optimized numerical tornado simulator and its application to transient wind-induced response of a long-span bridge. Journal of Wind Engineering and Industrial Aerodynamics 227, 105072. https://doi.org/10.1016/j.jweia.2022.105072

French, M.M., Kingfield, D.M., 2021. Tornado formation and intensity prediction using polarimetric radar estimates of updraft area. Weather and Forecasting 36 22112231. https://doi.org/10.1175/waf-d-21-0087.1

Gairola, A., Bitsuamlak, G., 2019. Numerical tornado modeling for common interpretation of experimental simulators. Journal of Wind Engineering and Industrial Aerodynamics 186, 32–48. https://doi.org/10.1016/j.jweia.2018.12.013

Gillmeier, S., Sterling, M., Hemida, H., Baker, C.J., 2018. A reflection on analytical tornado-like vortex flow field models. Journal of Wind Engineering and Industrial Aerodynamics 174, 10–27. https://doi.org/10.1016/j.jweia.2017.12.017

Gu, T.F., Liang, Y., Yan, Y.T., Jiang, W.J., Yue, H.Y., Hu, G., Zhang, J.Z., 2026. Towards high-fidelity urban wind profiles for the built environment: A neural field to fuse multi-source observational data in Guangzhou, China. Building and Environment 288, 114009. https://doi.org/10.1016/j.buildenv.2025.114009

Haan, F.L., Jr, Wang, J., Sterling, M., Kopp, G.A., 2024. Experimentally estimating wind load coefficients for tornadoes–An alternative perspective. Journal of Wind Engineering and Industrial Aerodynamics 251, 105811. https://doi.org/10.1016/j.jweia.2024.105811

Hadavi, M., Sun, L.T., Romanic, D., 2022. Normalized insured losses caused by windstorms in Quebec and Ontario, Canada, in the period 2008–2021. International Journal of Disaster Risk Reduction 80, 103222. https://doi.org/10.1016/j.ijdrr.2022.103222

Hangan, H., Kim, J.D., 2008. Swirl ratio effects on tornado vortices in relation to the Fujita scale. Wind and Structures 11, 291–302. https://doi.org/10.12989/was.2008.11.4.291

Hosseini, M.Y., Shiri, Y., 2024. Flow field reconstruction from sparse sensor measurements with physics-informed neural networks. Physics of Fluids 36, 073606. https://doi.org/10.1063/5.0211680

Hu, F., Li, Q.S., 2024. Reconstruction of tropical cyclone boundary layer wind field using physics-informed machine learning. Physics of Fluids 36, 116608. https://doi.org/10.1063/5.0234728

Huang, J.X., Li, Q.S., Han, X.L., 2024. Reconstruction of missing wind data based on limited wind pressure measurements and machine learning. Physics of Fluids 36, 076620. https://doi.org/10.1063/5.0220410

Ishihara, T., Oh, S., Tokuyama, Y., 2011. Numerical study on flow fields of tornado-like vortices using the LES turbulence model. Journal of Wind Engineering and Industrial Aerodynamics 99, 239–248. https://doi.org/10.1016/j.jweia.2011.01.014

Jiang, W.J., Zhang, J.Z., Li, Y.R., Zhang, D.Q., Hu, G., Gao, H.X., Duan, Z.D., 2024. Advancing storm surge forecasting from scarce observation data: A causal-inference based Spatio-Temporal Graph Neural Network approach. Coastal Engineering 190, 104512. https://doi.org/10.1016/j.coastaleng.2024.104512

Kawaguchi, M., Tamura, T., Kawai, H., 2019. Analysis of tornado and near-ground turbulence using a hybrid meteorological model/engineering LES method. International Journal of Heat and Fluid Flowing 80, 108464. https://doi.org/10.1016/j.ijheatfluidflow.2019.108464

Khodayar, M., Wang, J.H., 2019. Spatio-temporal graph deep neural network for short-term wind speed forecasting. IEEE Transactions on Sustainable Energy 10, 670–681. https://doi.org/10.1109/TSTE.2018.2844102

Kim, Y.C., Matsui, M., 2017. Analytical and empirical models of tornado vortices: A comparative study. Journal of Wind Engineering and Industrial Aerodynamics 171, 230–247. https://doi.org/10.1016/j.jweia.2017.10.009

Kurdzo, J.M., Nai, F., Bodine, D.J., Bonin, T.A., Isom, B., Palmer, R.D., Cheong, B.L., Lujan, J., Mahre, A., Byrd, A.D., 2017. Observations of severe local storms and tornadoes with the atmospheric imaging radar. Bulletin of the American Meteorological Society 98, 915–935. https://doi.org/10.1175/bams-d-15-00266.1

Lagerquist, R., McGovern, A., Homeyer, C.R., Gagne, D.J., Smith, T., 2020. Deep learning on three-dimensional multiscale data for next-hour tornado prediction. Monthly Weather Review 148, 2837–2861. https://doi.org/10.1175/mwr-d-19-0372.1

Lewellen, W.S., Lewellen, D.C., Sykes, R.I., 1997. Large-eddy simulation of a tornado's interaction with the surface. Journal of the Atmospheric Sciences 54, 581–605. https://doi.org/10.1175/1520-0469(1997)054<0581:lesoat>2.0.co;2

Li, Q.L., Wang, Z.T., Li, L., Hao, H., Chen, W.S., Shao, Y.D., 2023. Machine learning prediction of structural dynamic responses using graph neural networks. Computers Structures 289, 107188. https://doi.org/10.1016/j.compstruc.2023.107188

Ling, J.L., Kurzawski, A., Templeton, J., 2016. Reynolds averaged turbulence modelling using deep neural networks with embedded invariance. Journal of Fluid Mechanics 807, 155–166. https://doi.org/10.1017/jfm.2016.615

Liu, F.Y., Xu, Y.J., Li, J.L., Wang, L.B., 2025. Graph neural network–based spatiotemporal structural response modeling in buildings. Journal of Computing in Civil Engineering 39, 04025006. https://doi.org/10.1061/jccee5.cpeng-6229

Liu, K.J., Cai, Y., 2025. A deep convolutional generative adversarial network for data imputation: Application to wind speed time series. Advances in Wind Engineering 2, 100054. https://doi.org/10.1016/j.awe.2025.100054

Liu, Z.Q., Ishihara, T., 2015. A study of tornado induced mean aerodynamic forces on a gable-roofed building by the large eddy simulations. Journal of Wind Engineering and Industrial Aerodynamics 146, 39–50. https://doi.org/10.1016/j.jweia.2015.08.002

Maulik, R., San, O., Jacob, J.D., Crick, C., 2019. Sub-grid scale model classification and blending through deep learning. Journal of Fluid Mechanics 870, 784–812. https://doi.org/10.1017/jfm.2019.254

Natarajan, D., Hangan, H., 2012. Large eddy simulations of translation and surface roughness effects on tornado-like vortices. Journal of Wind Engineering and Industrial Aerodynamics 104106 577–584. https://doi.org/10.1016/j.jweia.2012.05.004

Özgenç, R., Ekmekcioğlu, Ö., Deniz, A., 2025. Revealing the economic consequences of tornadoes using a two-stage SVM-based predictive approach. Stochastic Environmental Research and Risk Assessment 39, 2395–2412. https://doi.org/10.1007/s00477-025-02975-5

Rankine, W.J.M., 1872. A manual of applied mechanics. Charles Griffin and Company, London.

Refan, M., Hangan, H., Wurman, J., 2014. Reproducing tornadoes in laboratory using proper scaling. Journal of Wind Engineering and Industrial Aerodynamics 135, 136–148. https://doi.org/10.1016/j.jweia.2014.10.008

Rohanizadegan, M., Petrone, R.M., Pomeroy, J.W., Kosovic, B., Muñoz-Esparza, D., Helgason, W.D., 2023. High-resolution large-eddy simulations of flow in the complex terrain of the Canadian Rockies. Earth and Space Science 10, e2023EA003166. https://doi.org/10.1029/2023ea003166

Rott, N., 1958. On the viscous core of a line vortex. Zeitschrift für Angewandte Mathematik und Physik ZAMP 9, 543–553. https://doi.org/10.1007/BF02424773

Rotunno, R., Bluestein, H.B., 2024. Recent developments in tornado theory and observations. Reports on Progress in Physics 87, 114801. https://doi.org/10.1088/1361-6633/ad7f6a

Rybchuk, A., Hassanaly, M., Hamilton, N., Doubrawa, P., Fulton, M.J., Martínez-Tossas, L.A., 2023. Ensemble flow reconstruction in the atmospheric boundary layer from spatially limited measurements through latent diffusion models. Physics of Fluids 35, 126604. https://doi.org/10.1063/5.0172559

Satrio, M.A., Bodine, D.J., Reinhart, A.E., Maruyama, T., Lombardo, F.T., 2020. Understanding how complex terrain impacts tornado dynamics using a suite of high-resolution numerical simulations. Journal of the Atmospheric Sciences 77, 3277–3300. https://doi.org/10.1175/jas-d-19-0321.1

Scarselli, F., Gori, M., Tsoi, A.C., Hagenbuchner, M., Monfardini, G., 2009. The graph neural network model. IEEE Transactions on Neural Networks 20, 61–80. https://doi.org/10.1109/TNN.2008.2005605

Sessa, M.F., Trapp, R.J., 2020. Observed relationship between tornado intensity and pretornadic mesocyclone characteristics. Weather and Forecasting 35, 1243–1261. https://doi.org/10.1175/waf-d-19-0099.1

Smith, B.T., Thompson, R.L., Speheger, D.A., Dean, A.R., Karstens, C.D., Anderson-Frey, A.K., 2020. WSR-88D tornado intensity estimates. Part I: Real-time probabilities of peak tornado wind speeds. Weather and Forecasting 35, 2479–2492. https://doi.org/10.1175/waf-d-20-0010.1

Snaiki, R., Wu, T., 2019. Knowledge-enhanced deep learning for simulation of tropical cyclone boundary-layer winds. Journal of Wind Engineering and Industrial Aerodynamics 194, 103983. https://doi.org/10.1016/j.jweia.2019.103983

Snaiki, R., Wu, T., 2022. Knowledge-enhanced deep learning for simulation of extra-tropical cyclone wind risk. Atmosphere 13, 757. https://doi.org/10.3390/atmos13050757

Sullivan, R.D., 1959. A two-cell vortex solution of the navier-stokes equations. Journal of the Aerospace Sciences 26, 767–768. https://doi.org/10.2514/8.8303

Tang, Z., Feng, C.D., Wu, L., Zuo, D.L., James, D.L., 2018. Characteristics of tornado-like vortices simulated in a large-scale ward-type simulator. BoundaryLayered Meteorology 166, 327–350. https://doi.org/10.1007/s10546-017-0305-7

Tang, Z., Zuo, D.L., James, D., Eguchi, Y., Hattori, Y., 2018. Effects of aspect ratio on laboratory simulation of tornado-like vortices. Wind and Structures 27, 111–121. https://doi.org/10.12989/WAS.2018.27.2.111

Tochimoto, E., 2022. Environmental controls on tornadoes and tornado outbreaks. AtmosphereOcean 60, 399–421. https://doi.org/10.1080/07055900.2022.2079472

Trafalis, T.B., Santosa, B., Richman, M.B., 2006. Learning networks for tornado detection. International Journal of General Systems 35, 93–107. https://doi.org/10.1080/03081070500502850

Trafalis, T.B., Santosa, B., Richman, M.B., 2016. Tornado detection with kernel-based classifiers from WSR-88D radar data. In: Kotsireas, I.S., Nagurney, A., Pardalos, P.M. (Eds.), Dynamics of disasters—Key concepts, models, algorithms, and insights. Springer International Publishing, pp. 329–344.

Vatistas, G.H., Kozel, V., Mih, W.C., 1991. A simpler model for concentrated vortices. Experiments in Fluids 11, 73–76. https://doi.org/10.1007/BF00198434

Wang, M.G., Cao, S.Y., Cao, J.X., 2022. Numerical study on applicability of various swirl ratio definitions to characterization of tornado-like vortex flow field. Journal of Wind Engineering and Industrial Aerodynamics 220, 104841. https://doi.org/10.1016/j.jweia.2021.104841

Ward, N.B., 1972. The exploration of certain features of tornado dynamics using a laboratory model. Journal of the Atmospheric Sciences 29, 1194–1204. https://doi.org/10.1175/1520-0469(1972)029<1194:teocfo>2.0.co;2

Wu, S.W., Sun, F., Zhang, W.T., Xie, X., Cui, B., 2022. Graph neural networks in recommender systems: A survey. ACM Computing Surveys 55, 1–37. https://doi.org/10.1145/3535101

Wu, T., Snaiki, R., 2022. Applications of machine learning to wind engineering. Frontiers in Built Environment 8, 811460. https://doi.org/10.3389/fbuil.2022.811460

Zhang, D.R., Roy, N., Wang, R.J., Frost, J.D., 2025. Predicting tornado-induced building damage: A comparative study of tree-based models and graph neural networks. International Journal of Disaster Risk Reduction 123, 105525. https://doi.org/10.1016/j.ijdrr.2025.105525

Zhang, H., Wang, H., Xu, Z.D., Khoo, B.C., 2023b. A novel three-dimensional analytical tornado model constructed based on force balance analysis. Physics of Fluids 35, 065133. https://doi.org/10.1063/5.0156170

Zhang, H., Wang, H., Xu, Z.D., Liu, Z.Q., Khoo, B.C., 2023c. Investigation of the fluctuating velocity in a single-cell tornado-like vortex based on coherent structure extraction. Physics of Fluids 35, 015135. https://doi.org/10.1063/5.0133107

Zhang, H., Wang, H., Xu, Z.D., Liu, Z.Q., Khoo, B.C., 2023a. A physics-informed neural network-based approach to reconstruct the tornado vortices from limited observed data. Journal of Wind Engineering and Industrial Aerodynamics 241, 105534. https://doi.org/10.1016/j.jweia.2023.105534

Zhao, L., Dong, X., Huang, S.K., Chen, M., Ge, Y.J., 2024. Tornado-induced instability assessment of super large hyperbolic reinforced concrete cooling towers. Engineering Structures 312, 118224. https://doi.org/10.1016/j.engstruct.2024.118224

Zhong, Y.H., Fukami, K., An, B., Taira, K., 2023. Sparse sensor reconstruction of vortex-impinged airfoil wake with machine learning. Theoretical and Computational Fluid Dynamics 37, 269–287. https://doi.org/10.1007/s00162-023-00657-y

Zhou, X., Yang, L., Ma, S.Q., Wang, R.F., Li, Z.M., Song, Y.C., Gao, Y.S., Xu, J.Y., 2025. Analysis of the dynamic process of tornado formation on 28 July 2024. Remote Sensing 17, 2615. https://doi.org/10.3390/rs17152615

Zuo, D.L., Tang, Z., Zhang, H., James, D., Eguchi, Y., 2021. Narrowband components in two-celled tornado-like vortices generated in a Ward-type simulator. Journal of Wind Engineering and Industrial Aerodynamics 218, 104767. https://doi.org/10.1016/j.jweia.2021.104767